Cyclic Plasma Halogenation of Amorphous Carbon for Defect-Free Area-Selective Atomic Layer Deposition of Titanium Oxide

Mikhail Krishtab, Silvia Armini, Johan Meersschaut, Stefan De Gendt, and Rob Ameloot*

ABSTRACT: As critical dimensions in integrated circuits continue to shrink, the lithography-based alignment of adjacent patterned layers becomes more challenging. Area-selective atomic layer deposition (ALD) allows circumventing the alignment issue by exploiting the chemical contrast of the exposed surfaces. In this work, we investigate the selective deposition of TiO_2 by plasma halogenation of amorphous carbon (a-C:H) acting as a growth-inhibiting layer. On a-C:H, a CF_4 or Cl_2 plasma forms a thin halogenated layer that suppresses the growth of TiO_2, while nucleation remains unaffected on plasma-treated SiO_2. The same halogenating plasmas preferentially etch TiO_2 nuclei over films and thus enable the restoration of the halogenated surface of amorphous carbon. By embedding the intermediate plasma treatments in the ALD TiO_2 sequence, an 8 nm TiO_2 layer could be deposited with a selectivity of 0.998. The application of the cyclic process on a 60 nm half-pitch line pattern resulted in the defect-free deposition of TiO_2 at the bottom of the trenches. Cyclic fluorination demonstrated better growth inhibition compared to chlorination due to more efficient defect removal and retention of the favorable surface composition during plasma exposure. While exploring the TiO_2 nucleation defects at the limit of detection for conventional elemental analysis techniques ($<1 \times 10^{14}$ at/cm^2), we additionally highlight the value of imaging techniques such as atomic force microscopy for understanding defect formation mechanisms and accurately assessing growth selectivity.

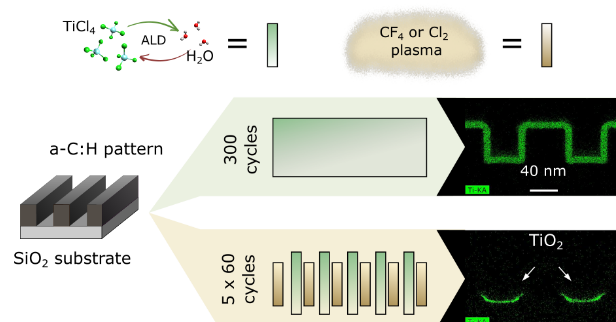

The relentless miniaturization of integrated circuits (ICs) for nearly half a century has increased the transistor count per chip from a few thousand to several billion. However, the cost and effort required for the continuation of Moore's law are rising rapidly.[1−3] As lateral dimensions approach 30 nm, the variability intrinsic to even the most advanced implementations of fabrication processes, including lithography, deposition, and etch, decreases the device yield due to pattern placement errors.[4] To address these challenges, novel patterning schemes based on the self-alignment of successively deposited device layers were developed. These approaches selectively form the next functional layer based on the underlying pattern, thus significantly improving the edge placement error margin.[5,6] One of the key enabling technologies in this context is area-selective deposition (ASD), which exploits differences in surface chemistry to grow only on the desired region of a patterned substrate. For several decades already, this technology has been used for the selective epitaxial growth of semiconductors and the formation of low-resistance contacts via chemical vapor deposition (CVD).[7,8] The recent intensification of ASD research is mainly associated with atomic layer deposition (ALD), a process that has rapidly gained importance in the last 2 decades.[9,10] The key principle of any ALD process lies in the separation of the growth reaction into half-reactions taking place sequentially on the exposed surfaces. The exceptional conformality and thickness control were responsible for the initial success of ALD in the semiconductor technology. In turn, the intrinsic surface sensitivity of ALD favors its application in resolving the current ASD challenges.[11−13]

A crucial parameter of an ASD process is its deposition selectivity, determined by the difference in the growth rate on growth and nongrowth surfaces.[8,12] Considering the critical dimensions of advanced ICs, even a few nuclei in the wrong location undermine the fabrication yield. For example, for another bottom-up patterning approach, directed self-assembly

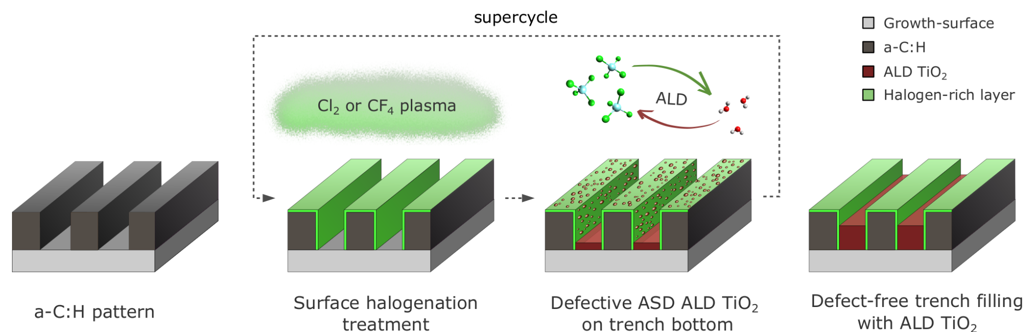

Figure 1. Defect-free ASD of ALD TiO_2 based on repetitive plasma halogenation of a-C:H.

(DSA) of block-copolymers,[14,15] the often-cited criterion is one or less defect per 100 cm^2.[16] Although in the context of the ASD, this requirement could be somewhat alleviated depending on the type and size of the growth defects as well as on the application, it is clear that the search for defect-free deposition schemes should be prioritized. ASD selectivity can be enhanced by suppressing nucleation on nongrowth surfaces or by removing defect nuclei on the latter surfaces through etching.[17] Examples of the first approach include regular self-assembled monolayer restoration steps via the dosing of the monolayer precursor[18] and the application of volatile growth-inhibiting adsorbate molecules supplied to the reactor before each ALD cycle.[19,20] Despite the positive impact of these approaches on the deposition selectivity, they cannot fully exclude nuclei on the nongrowth surface originating from nonidealities of the ALD process. Among the second group of methods, those based on intermediate etching represent a robust way to eliminate defects and allow a significant and, in theory, an infinite extension of the selectivity window. The intrinsic challenge of these approaches is that defect etching should occur selectively, that is, with minimal effect on the exposed growth and nongrowth surfaces. There are only a few studies that successfully demonstrate such approaches for the selective deposition of Ru and TiO_2.[21−25] It is worth noting that the ultimate selectivity of the etching process demonstrated in the work of Song et al. by a thermal atomic-layer etching of TiO_2 was not sufficient to ensure a defect-free ASD process due to the gradual degradation of the growth-inhibiting Si−H-terminated substrate.[23] Therefore, intermediate etching should ideally combine selective defect removal with the restoration of the nongrowth surface. Leveraging the surface mobility of unwanted nuclei is an alternative approach to facilitate defect elimination from the nongrowth area.[26,27] However, this surface diffusion phenomenon has been observed mostly for selective metal deposition processes and might not be universally applicable.

In this work, we propose and explore a new robust scheme for the ASD of ALD TiO_2 on SiO_2 in the presence of hydrogenated and patterned amorphous carbon (a-C:H) as a growth-inhibiting layer (Figure 1). In advanced patterning, a-C:H is a common hard-mask (HM) material valued for its uniform composition, high mechanical strength, good etch selectivity, and ashability.[28−30] Another advantage of a-C:H is that its surface can be modified in various ways by plasma treatment.[31,32] Though often neglected in microelectronic fabrication, this property is particularly beneficial with respect to ASD because a simple plasma treatment can switch the a-C:H surface between growth-inhibiting and growth-enhancing. The first realizations of this concept were based on the plasma hydrogenation of a-C:H films. As deposited, the a-C:H coating contains numerous sp^2/sp^3 motifs, some of which are unstable and react with moisture upon contact with air.[33,34] The chemisorbed oxygen species provide nucleation sites for ALD. Exposure to H_2 or remote He/H_2 plasmas reduces the oxygen content in the topmost surface layer, thus delaying the nucleation of ALD TiN, TiO_2, HfO_2, and ALD Ru.[35,36] However, despite encouraging results on blanket a-C:H coatings, the hydrogenation plasma alone is neither able to extend the demonstrated selectivity window nor prevent excessive defect nucleation on patterned a-C:H due to residues inherited from other fabrication steps. To address these challenges, we functionalized a-C:H films with halogen-based plasmas such as Cl_2 and CF_4 to reduce the accessibility of the oxygen sites by the formation of a thin top layer enriched with CCl_x and CF_x groups. Because these plasmas also etch metal oxides and nitrides, repetitive plasma halogenation treatments were studied as part of a supercycle approach. The resulting AS-ALD TiO_2 scheme was verified on both blanket substrates and 60 nm half-pitch patterned test structures.

EXPERIMENTAL DETAILS

Deposition of Amorphous Carbon Films. 100 nm thick films of hydrogenated amorphous carbon (a-C:H) were deposited on 300 mm p-Si(100) wafers in a Producer platform from Applied Materials. The a-C:H films formed via plasma-enhanced CVD (PE-CVD) serve as carbon HM layers in various patterning schemes. The deposition was done in a plasma of helium (He) and methylacetylene (C_3H_6). The resulting layers have a density of 1.46 g/cm^3 as measured by X-ray reflectometry and contain 45 at./% hydrogen according to elastic recoil detection analysis.[37] The pristine a-C:H material has a sp^3/sp^2 ratio of 1.11 according to the analysis of the carbon KLL Auger peak (Figure S1).[38] The films contain traces of oxygen originating from postdeposition oxidation.

Plasma Treatment. The exposure of a-C:H films to the plasma was carried out in two different chambers connected to a single etch platform, which allows transferring 300 mm wafers between the process chambers without air exposure. The first chamber was used to process wafers heated to 100 °C with a remote He/H_2 plasma (1 Torr, 2800 sccm He, 200 sccm H_2, 2 kW). The plasma was ignited in the top part of the processing chamber, separated from the wafer by a grid that filters out charged species and photons. In the second chamber, a magnetically enhanced capacitively coupled plasma (ME-CCP) reactor was used to ignite low-power Cl_2 or CF_4 plasmas for the surface halogenation of a-C:H films and etching TiO_2 nucleation defects. Both plasma processes were run under the same conditions: 150 W, 100 mTorr, and 150 sccm of Cl_2 or CF_4. The temperature of the wafers during the halogenating plasma treatment was maintained at 30 °C.

ALD of TiO_2. The growth of TiO_2 was realized by two ALD processes featuring different titanium precursors and deposition platforms. The default ALD TiO_2 process based on $TiCl_4$/H_2O was

implemented in an industrial showerhead-type ALD reactor. The process included a 1 min annealing step at a susceptor temperature of 200 °C, followed by alternating precursor pulses (200 ms $TiCl_4$, 600 ms H_2O) separated by 6 s Ar purge steps if not mentioned otherwise. This process was used throughout the work for the deposition of TiO_2 unless stated otherwise. Another ALD TiO_2 process based on titanium(IV)isopropoxide (TTIP)/H_2O was implemented in a customized Savannah S200 reactor from Veeco. The chuck temperature was maintained at 200 °C during the ALD process as well as during the 2 min substrate pre-annealing. The pulse scheme consisted of 2 s TTIP and 5 s of H_2O injections, each followed by N_2 purge steps of 30 s.

Preparation of Patterned Test Structures. The process flow for the preparation of 60 nm half-pitch line patterns of a-C:H on a Si-substrate is depicted in Figure S2. The processing route involved film stack deposition, immersion 193 nm lithography, dry etch patterning, and wet removal of the HM film. The stack was formed by depositing 20 nm PE-CVD SiO_2 HM over a 70 nm a-C:H layer. After the HM opening with the CF_4/CHF_3/Ar plasma, the a-C:H film was patterned by a H_2/N_2 capacitively coupled discharge. The residual SiO_2 HM was etched away by the exposure of the wafer top side to 0.5% aqueous solution of hydrofluoric acid (HF) for 60 s.

Characterization. *Static Water Contact Angle.* The static water contact angle (WCA) was measured with an OCA 230L optical contact angle measuring and contour analysis system from DataPhysics equipped with a CCD camera and a Hamilton 500 μL syringe. The recorded images of 2 μL water droplets (4 per sample) were analyzed with the ellipse fitting model in the DataPhysics SCA20 software to extract static contact angles.

X-ray Reflectometry. X-ray reflectometry (XRR) measurements were performed on a Bede Metrix-L diffractometer equipped with a Cu Kα source (Jourdan Valley). The intensity of the specularly reflected X-rays was recorded by symmetrically scanning the X-ray incidence angle (between the X-rays and the sample surface) from 400 to 16,000 arcsec together with the detector position. The obtained X-ray reflectivity data were fitted using Bede REFS software with a three-layer model including a Si-substrate. The Bede REFS fitting algorithm was also used to estimate the standard (1σ) errors on the obtained thickness values.

X-ray Photoelectron Spectroscopy. X-ray photoelectron spectroscopy (XPS) measurements were carried out at two exit angles (measured from the sample normal) using a Theta300 system from Thermo Fisher Scientific. While the spectra recorded at an exit angle of 78° conveyed information about the elemental composition of the topmost surface, the spectra recorded at 22° included the signal from the bulk composition of the a-C:H films. The measurements were performed using a monochromatized Al K_α X-ray source (1486.6 eV) and a spot size of 400 μm. Standard sensitivity factors were used to convert peak areas to atomic concentrations. Therefore, the measured concentrations might deviate from reality (up to 20%). However, when atomic concentrations are compared between the probed surfaces, the results are more accurate. Long-term repeatability of composition analysis has been shown to be ~1% deviations (according to the regularly measured composition of a HfSiO sample serving as an internal standard).

Time-of-Flight Secondary Ion Mass Spectroscopy. Time-of-flight secondary ion mass spectroscopy (TOF SIMS) was performed in a TOF-SIMS IV system from ION-ToF GmbH. The mass spectra of negatively charged secondary ions were collected from an area of 250 μm × 250 μm with a Bi^{3+} 25 keV primary beam (~0.2 pA). The signals for negative ions of interest were reported as integrals over the respective mass to charge ratios. These values were used for the qualitative comparison of species and their concentrations on surfaces of similar compositions (i.e., chlorinated and fluorinated a-C:H layers, respectively).

Spectroscopic Ellipsometry. Spectroscopic ellipsometry (SE) measurements were performed on films of a-C:H and ALD TiO_2 to assess their etch rate in the halogenating plasmas. The Psi/Delta spectra were captured in the wavelength range of 400−800 nm using an M-2000 ellipsometer from J. A. Woollam. The spectra were fitted in CompleteEASE software with an optical model comprising a Si-substrate, a 1.5 nm native SiO_2, and a Cauchy layer with variable thickness and optical parameters.

Rutherford Backscattering Spectroscopy. Rutherford backscattering spectroscopy (RBS) measurements were used to quantify the amount of TiO_2 deposited on the surfaces of interest and performed in a random rotation mode using 1.5 MeV He^+ ions from a 6SDH tandem accelerator (National Electrostatics Corporation) equipped with an Alphatross ion source. The experimental end-station was a 5-axis goniometer developed at the Forshungszentrum Jülich. The angle between the sample normal and the beam was set to 11°. The solid angle of the PIPS detector was 0.42 msr, the scattering angle was 170°. The beam spot was confined to 1 × 1 mm^2. In-house developed analysis software was used to fit the spectra and to deduce the areal density. To calculate the Ti areal density, we assumed a TiO_2 density equal to that of anatase (3.78 g/cm^3), as suggested by a previous study on $TiCl_4$/H_2O ALD.[39] This assumption is also supported by the good agreement between the RBS-derived thickness of the ALD TiO_2 grown on native SiO_2 and the corresponding ellipsometry analysis (Figure S3). The experimentally determined RBS detection limit for the Ti signal is $\sim 1 \times 10^{14}$ at/cm^2, which is equal to 0.035 nm TiO_2.

Atomic Force Microscopy. Atomic force microscopy (AFM) topography images (1 μm × 2 μm, 256 × 512 pixels) were recorded in the tapping mode with a Dimension Edge microscope (Bruker). Image corrections (rows alignment, horizontal scars elimination) and plottings were performed with Gwyddion 2.44 software.[40] The latter was used to calculate the root-mean-squared (RMS) surface roughness and analyze the TiO_2 nuclei. In this work, a grain was defined as at least one pixel (3.9 nm × 3.9 nm) in the topography map with a height exceeding the 2 × 5σ threshold, where σ is the RMS value of the a-C:H surface before the deposition of TiO_2 and the map data are levelled by setting the minimum height value to zero. The chosen height threshold guarantees that the detected grains are not associated with the roughness of the a-C:H surface and thus allows a consistent comparison between samples. Although defects below the threshold height are not taken into account, the sensitivity of this approach is noticeably better than top-down SEM image analysis (Figure S4). More importantly, the AFM metrology provides height information for individual TiO_2 nuclei, which allows a better understanding of the defect evolution during the growth and etch processes.

Scanning Electron Microscopy. Cross-section and top-down scanning electron microscopy (SEM) images were collected on manually cleaved samples with a Hitachi SU8000 microscope operating at 10 kV and with a secondary electron detector. No charge-reducing metal layer was sputtered to avoid ambiguity during the analysis of TiO_2 nuclei. The detection and counting of TiO_2 grains on the surface of halogenated a-C:H were performed with ImageJ v. 1.52d based on the manually adjusted color threshold.[41]

Transmission Electron Microscopy. Transmission electron microscopy (TEM) analysis of an a-C:H line pattern cross section was done on 30−50 nm thick lamellas prepared with a dual-beam FIB/SEM Helios NanoLab 450HP (FEI). Before FIB lift-out, the top surface of the samples was sequentially coated with three layers which are as follows: a thin layer of e-beam Pt (stray e-Pt deposition), a drop-casted organic layer (spin-on carbon) soft-baked at 150 °C, and an ion-beam (30 kV)-deposited Pt layer. As the last step of the lamella preparation, there was a 5 kV ion beam milling step to reduce the FIB-induced surface damage. The TEM images and energy-dispersive X-ray spectroscopy (EDS) element maps were captured with a Titan3 G2 60-300 transmission electron microscope (FEI) operating at 200 kV.

RESULTS AND DISCUSSION

Plasma Halogenation of a-C:H. The first step toward the implementation of the proposed AS-ALD scheme is the optimization of the a-C:H plasma halogenation. The evolution of the structure and surface composition of the 100 nm a-C:H layer was studied upon applying low-power Cl_2 or CF_4 plasmas

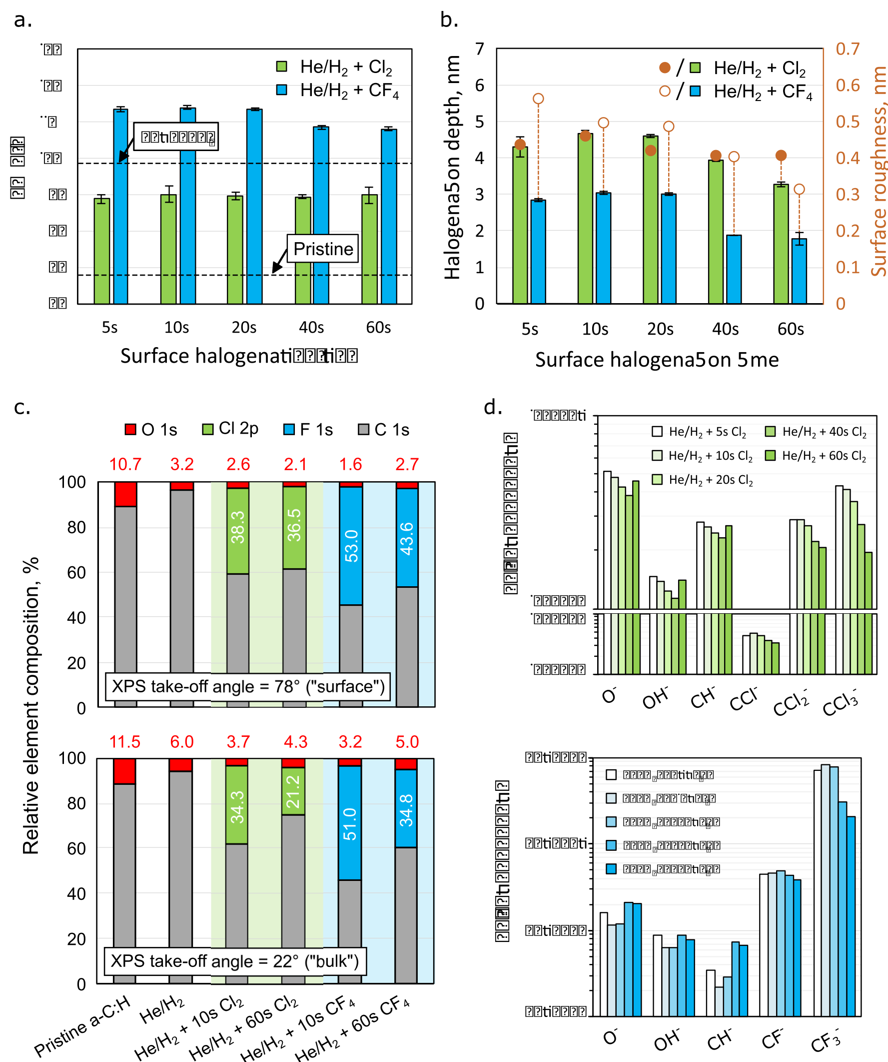

Figure 2. Characterization of a-C:H surfaces after the plasma halogenation: (a) WCA; (b) thickness of the halogen-rich layer, as determined via XRR; (c) elemental composition of the a-C:H film surface by XPS at take-off angles of 22 and 78°, corresponding to different probe depths; and (d) chemical composition of chlorinated and fluorinated a-C:H assessed by TOF-SIMS. The signals from the major species detected are represented. The CF_2^- signal is missing due to detector saturation.

ignited in an industrial ME-CCP reactor (Figure 2). The halogenation treatment was preceded by exposure of the a-C:H films to 30 s of the remote He/H_2 plasma to remove approx. 2 nm of the oxygen-rich layer, as in the work of Stevens et al.[36] This pretreatment with H-radicals results in a 1−2 nm strongly hydrogenated surface layer.[42] The surface hydrogenation translated into an enhanced hydrophobicity (see dashed lines in Figure 2a) and an approximately threefold reduced oxygen content (Figure 2c).

Exposing pretreated a-C:H to a Cl_2 or CF_4 plasma induced the formation of a surface layer enriched with the respective halogen species and a further reduced oxygen content (Figure 2c). Following the shortest tested treatment of 5 s, the thicknesses of the chlorinated and fluorinated layers estimated by XRR were 4.3 and 2.8 nm, respectively (Figure 2b). The WCA of the chlorinated a-C:H reached 90°, while the hydrophobicity of the fluorinated a-C:H surface (WCA of 113°) approached that of PTFE and perfluoroalkyl-terminated SAMs (Figure 2a).[43,44] For both types of halogenating plasma, extended exposure (40 s and longer) decreases the halogen-rich layer thickness by ∼1 nm, as evidenced by XRR (Figure 2b). This evolution is also evident from XPS measurements at a 22° take-off angle, from the reduced chlorine and fluorine content when comparing 10 and 60 s exposures. In both cases, the drop in the halogen concentration indicates the start of the etching.

To further understand the effect of the plasma halogenation on the composition of a-C:H, the surface was analyzed by TOF-SIMS (Figure 2d). Both chlorinated and fluorinated a-C:H surfaces were changing as a function of the plasma treatment time. The detected species can be grouped into two categories: (1) species originating from the pristine a-C:H and (2) fragments of halogenated carbon. The changes in the first group, including O^-, OH^-, and CH^-, are well correlated, and their initial decrease followed by an increase at longer treatment times is likely related to the increase and decrease in the halogenation depth, respectively. In the second category, consisting of CX_n^- ions (X = Cl, F; n = 1, 2, 3), the most prominent trend is the strong reduction of terminal CF_3 and CCl_3 species. The high concentration of these terminal groups after the first seconds of halogenation can be related to the efficient and complete H abstraction from the methyl groups

on the a-C:H surface. The density of the latter is increased during the He/H_2 plasma pretreatment. Similar halogenation reactions were observed for methyl-containing organosilica dielectrics under a high dose of fluorine radicals.[45,46] With the onset of a-C:H etching, the concentration of the terminal groups reduces as deeper layers not affected by the He/H_2 treatment get in contact with the halogenating plasma.

Growth-Blocking Mechanism of Halogenated a-C:H. The halogenated a-C:H films were subjected to 200 $TiCl_4$/H_2O ALD cycles. As shown in the AFM grain maps (Figure 3), TiO$_2$ formed islands on the halogenated a-C:H surfaces consistent with the expected suppressed nucleation. However, the efficiency of growth blocking, estimated by the area covered by TiO_2, strongly depended on the type of halogenating plasma as well as its duration. In the case of a Cl_2 plasma, shorter surface treatments resulted in more efficient growth inhibition. In contrast, a-C:H surfaces functionalized by a CF_4 plasma showed the lowest defect nucleation density after longer treatment times.

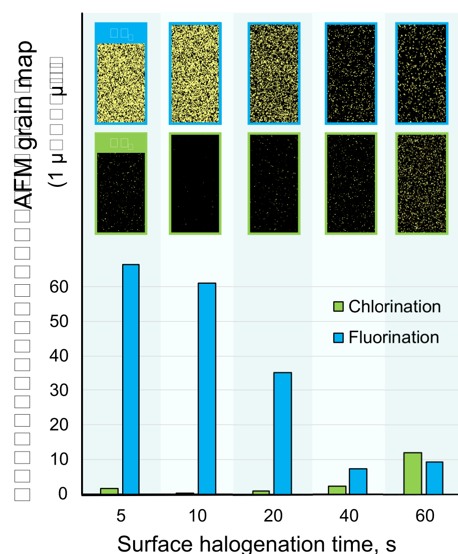

Figure 3. Influence of the surface halogenation duration on TiO_2 growth inhibition, assessed via grain analysis of AFM images after 200 $TiCl_4$/H_2O cycles. The bottom part of the chart shows the projected areas of the TiO_2 grains in the AFM grain maps above the corresponding bars.

To understand the determining factors in TiO_2 nucleation, we first excluded the degradation of the halogenated a-C:H surface during ALD by testing its thermal stability and potential reactivity toward H_2O and $TiCl_4$ precursors (Figures S5 and S6). Dependency on the metal−organic precursor was ruled out by using titanium(IV)isopropoxide instead of $TiCl_4$ (Figure S6). Because oxygen-containing functional groups (e.g., C═O and C−OH) act as nucleation sites in AS-ALD TiO_2 on hydrogenated a-C:H[36] and halogen-containing groups do not react with the ALD precursors under the tested conditions, we assume the former to be the cause of defect nucleation on halogenated a-C:H. However, neither XPS nor TOF-SIMS indicate a higher surface concentration of oxygen in fluorinated versus chlorinated a-C:H, even though the former shows significantly more TiO_2 nuclei. Therefore, the difference in defect nucleation could originate from differences in the accessibility of the oxygen sites by the ALD precursor.

Given the relatively high oxygen content in the pristine a-C:H, the top oxygen-depleted halogenation layer could act as a barrier against the diffusion of the precursor into the film, analogous to PMMA or PVP films in previous AS-ALD TiO_2 studies.[47−49] To test this hypothesis, we studied the effect of the substrate temperature during ALD (Figure 4). The strong

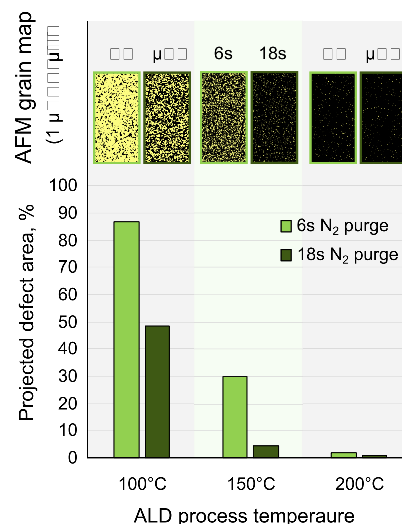

Figure 4. Effect of the substrate temperature and N_2 purge time within an ALD cycle on TiO_2 growth inhibition on a-C:H subjected to 10 s of chlorination. Top: growth inhibition assessed via grain analysis of AFM images after 250 $TiCl_4$/H_2O cycles. Bottom: projected areas of the TiO_2 grains in the AFM grain maps above the corresponding bars.

suppression of TiO_2 nucleation on the chlorinated a-C:H surface at higher temperatures rules out sub-surface growth.[50] The observed temperature dependence, together with the positive effect of a prolonged N_2 purge (Figure 4), indicates the dominant effect of the precursor adsorption and diffusion kinetics. By correlating the changes in the composition of the halogenation layer with the growth defectivity, as shown in Figure 3, we identified the factors that contribute to less accessible oxygen sites. In the case of the Cl_2 plasma, deeper chlorination and surface enrichment with bulky terminal $-CCl_3$ groups are favorable because of a reduction in surface O-sites and steric hindrance, respectively. The major factor benefiting growth inhibition on fluorinated a-C:H appears to be the formation of a cross-linked fluorocarbon layer with few terminal $-CF_3$ groups. Guided by these insights, we chose the two extreme treatment times of the explored timescale as reference halogenation conditions, 10 and 60 s for the Cl_2 and CF_4 plasma, respectively.

AS-ALD TiO_2 Growth Curve. The TiO_2 thickness as a function of the ALD cycle number on pristine and halogenated SiO_2 and a-C:H surfaces is shown in Figure 5a. The growth on the native SiO_2 is linear with a growth per cycle (GPC) of 0.035 nm/cycle. Exposure to the halogenating plasma does not cause any nucleation delay for the native SiO_2 surface, likely because of the fast hydrolysis of the formed Si−Cl and Si−F bonds in air or during the first H_2O ALD pulse (Figure S7, Table S1). The growth on nontreated a-C:H is only slightly delayed, in clear contrast with the same layer exposed to a Cl_2 or CF_4 plasma. While the nucleation delay on halogenated a-C:H is captured by both RBS and AFM (Figure 5), the latter provides more detailed information about the process

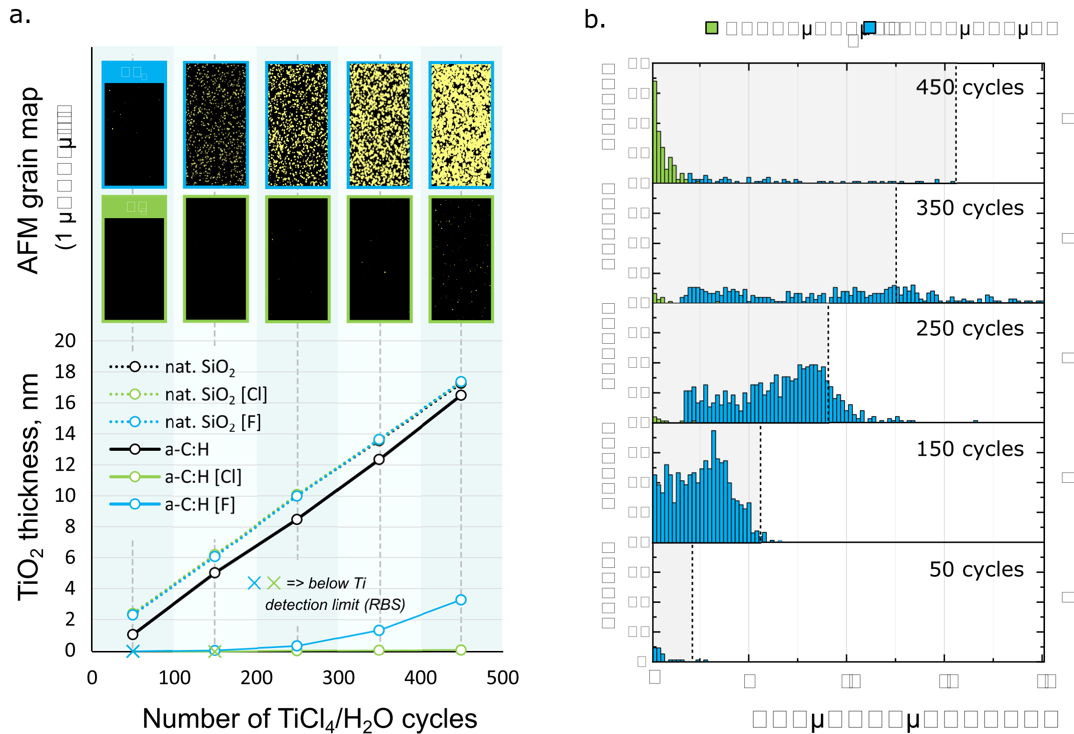

Figure 5. ALD TiO_2 ($TiCl_4$/H_2O) on various surfaces. (a) Thickness of TiO_2 on the growth (native SiO_2) and nongrowth surfaces (a-C:H) subjected to plasma halogenation and different numbers of ALD cycles. The thickness values were estimated by ellipsometry (growth areas) and based on the RBS Ti areal density (nongrowth areas). The top part of the chart shows AFM grain maps of the nongrowth surfaces demonstrating the spatial distribution of TiO_2 nuclei (highlighted in yellow). (b) Height distribution of TiO_2 nucleation defects formed on the halogenated a-C:H surfaces, as estimated by grain analysis of AFM surface topography images. The height values exclude the $2 \times 5\sigma$ threshold (3.60 and 3.94 nm for the chlorinated and fluorinated a-C:H, respectively; 5.5 nm for 250−450 ALD cycle processes on fluorinated a-C:H). The dotted lines indicate the corresponding TiO_2 thickness on SiO_2.

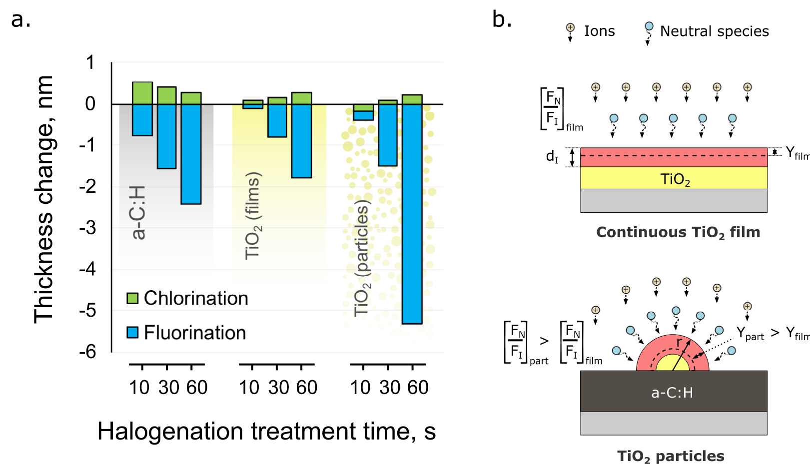

Figure 6. Halogen plasma etching of TiO_2 films and particles. (a) Change in the thickness of a-C:H and TiO_2 films (based on ellipsometry) and the average height of TiO_2 nuclei (based on AFM grain analysis) upon different Cl_2 or CF_4 plasma treatment times. (b) Mechanism of the TiO_2 film and particle etching in a reactive ion etching (RIE) plasma. The interfacial damage layer (d_I) and intact TiO_2 material are shown in red and yellow, respectively. In both scenarios, the layer removed by plasma etching per unit time (Y) is indicated by a dashed line. The higher etch rate in the RIE plasma is associated with a larger neutral-to-ion flux ratio (F_N/F_I).

selectivity.[51] For example, the AFM grain maps shown in Figure 5a show the presence of TiO_2 at a sensitivity level where no Ti signal is detected by RBS yet. In addition, the topography information in AFM enables monitoring TiO_2 nucleation quantitatively, as exemplified by Figure 5b showing that the number of nucleation defects is not fixed but continuously grows. This continuous defect generation could be associated with sub-optimal ALD process conditions,[25,52] for example, by insufficiently long purging to remove physisorbed precursor or reaction byproducts, as shown in Figure 4. The defect distribution on chlorinated a-C:H suggests an acceleration in new nuclei formation as the ALD process proceeds, possibly due to the retention and accumulation of the adsorbed species over several ALD cycles before forming new nuclei. In contrast, on fluorinated a-C:H, the continuous formation of new nuclei is accompanied by the

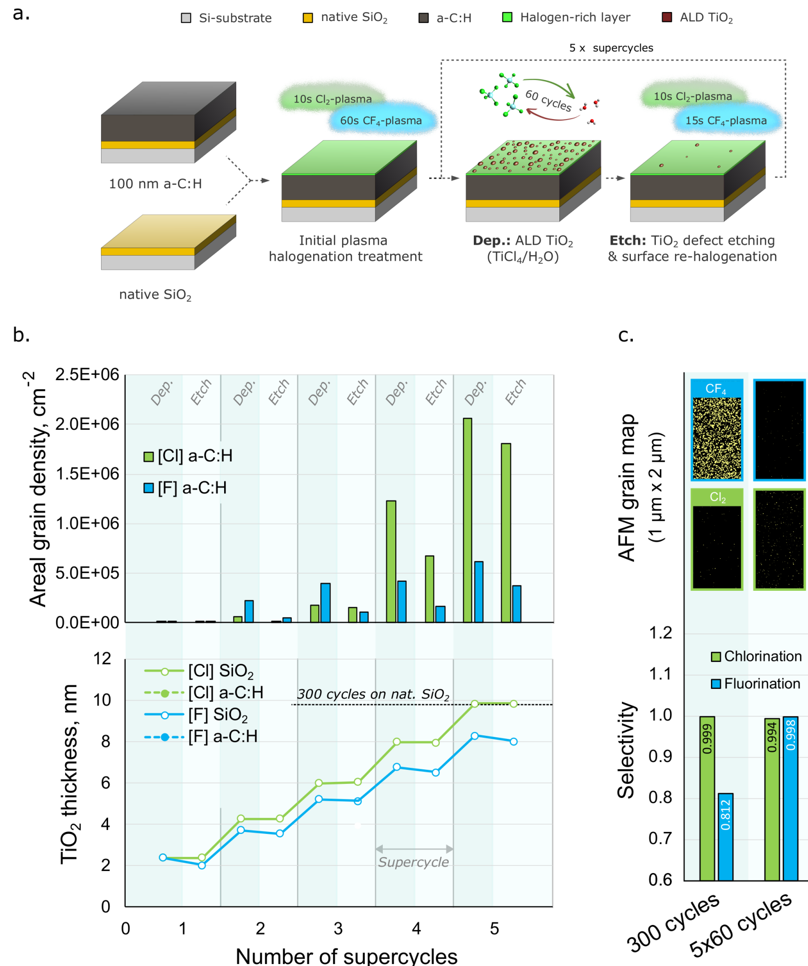

Figure 7. Cyclic plasma halogenation for AS-ALD TiO_2 on blanket growth (SiO_2) and nongrowth (halogenated a-C:H) surfaces. (a) Process flow of the AS-ALD supercycle approach. (b) Thickness of TiO_2 on SiO_2 (by ellipsometry), along with TiO_2 nuclei areal density on the halogenated a-C:H nongrowth surfaces (by AFM analysis) after each step within a five-supercycle process. (c) Bottom part of the chart shows the growth selectivity for a continuous ALD TiO_2 process and for one divided in five supercycles. The corresponding AFM grain maps in the top part show the TiO_2 nuclei (highlighted in yellow) on the halogenated a-C:H nongrowth surfaces.

growth of the nuclei already present, as indicated by a gradual shift of the grain height distribution to larger values (50−250 cycles). At 350 and more ALD cycles, the agglomeration of TiO_2 nuclei results in heights noticeably exceeding the film thickness on the SiO_2 growth surface. Considering that TiO_2 nuclei were growing rather uniformly during the first 250 ALD cycles, we neglect the contribution of nuclei diffusing over the fluorinated a-C:H surface in our discussion on the growth selectivity. To further minimize the impact of diffusion phenomena, which would lead to larger defects and hindered defect etching, the ALD process was limited to 200 cycles in the following experiments.

Plasma Etching of TiO_2 Defects. Although the deposition selectivity can likely be improved by reducing the dose of the metal−organic precursor,[52] we explored the etching capability of the halogenating plasmas as part of the ALD TiO_2 process to correct the imperfect growth inhibition. Cl_2 and CF_4 plasmas are commonly employed for etching metals, oxides, and nitrides, including TiO_2. However, the application of these plasmas for ASD defect removal requires that the halogenating plasma not only etches the undesired material formed on the nongrowth surface but also does so selectively with respect to other exposed surfaces. In the ASD scheme proposed in Figure 1, this requirement translates to the preferential etching of TiO_2 particles on halogenated a-C:H compared to continuous TiO_2 films on the SiO_2 growth area, or a-C:H itself. While evaluating thickness changes in films is straightforward (e.g., by ellipsometry), measuring TiO_2 particles on halogenated a-C:H is more intricate. Unlike ellipsometry or RBS, AFM measurements yield grain height statistics, which allow a reliable assessment of the grain etch rate (Figure S8). Therefore, AFM analysis was performed for halogenated a-C:H surfaces sequentially subjected to 200 $TiCl_4/H_2O$ cycles and Cl_2 or CF_4 plasma for different durations.

Figure 6a compares the impact of CF_4 and Cl_2 plasmas on the thickness of a-C:H, TiO_2 film, and TiO_2 grains. Both plasmas demonstrate the ability to etch these materials. However, for the Cl_2 plasma, material removal is less apparent due to the slow onset of steady-state etching and post-treatment oxidation in air due to the facile hydrolysis of surface Ti−Cl bonds. In contrast, the CF_4 plasma showed pronounced etching due to the more reactive F-radicals.[53] While no etch selectivity was observed between the a-C:H and TiO_2 films, the etch rate of the TiO_2 grains was nearly twice as high. This characteristic is essential to remove TiO_2 grains that can exceed the thickness of the desired TiO_2 layer (Figure 5b).

To understand this shape-selective etching, one should compare the impact of plasma species on a planar surface and

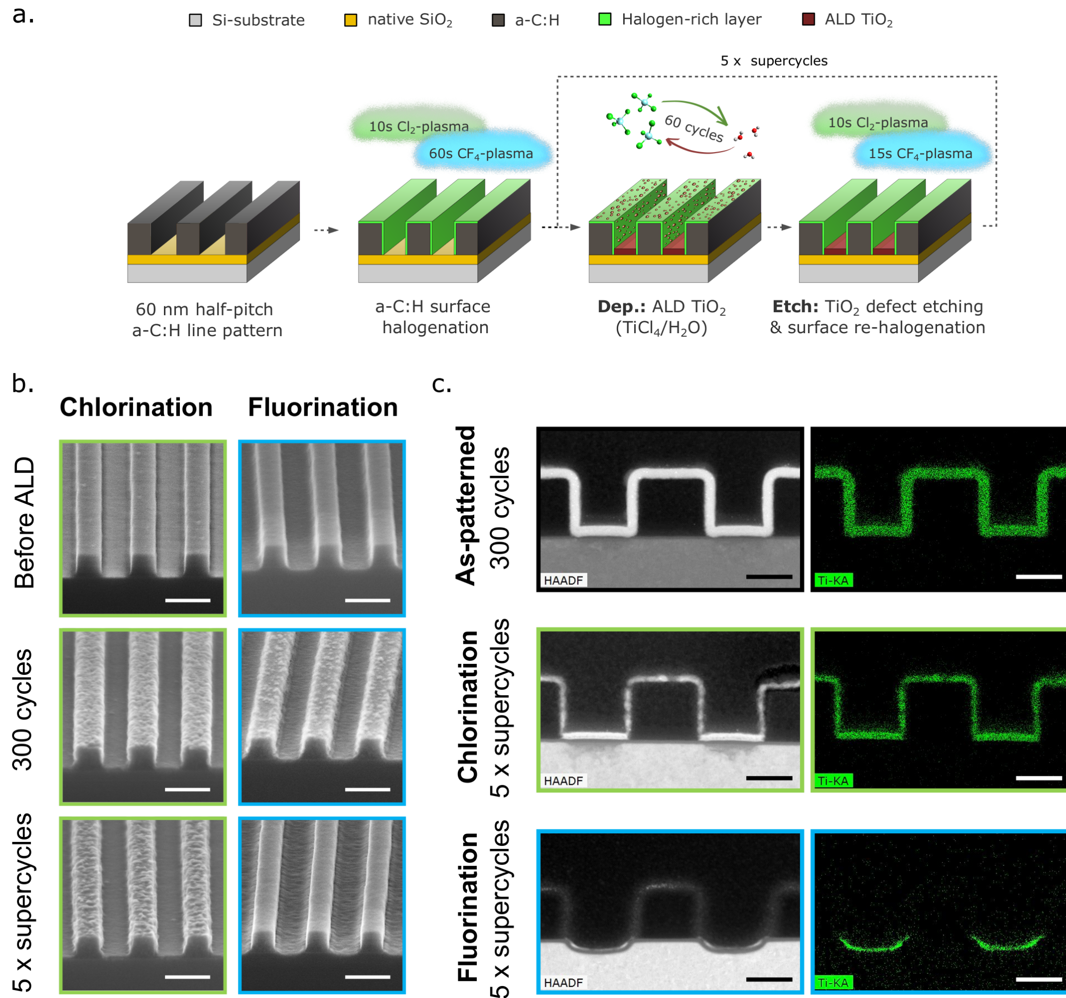

Figure 8. AS-ALD TiO_2 at the bottom of 60 nm half-pitch a-C:H patterns on SiO_2. (a) Experiment process flow. (b) Tilted cross-section SEM images of halogenated a-C:H line patterns before and after ALD TiO_2. Scale bar: 200 nm. (c) TEM−HAADF images and TEM−EDS Ti K_α maps of lamellas cut out perpendicularly to the a-C:H line pattern following ALD TiO_2. Scale bar: 40 nm.

on a particle (Figure 6b). According to molecular dynamics simulations reported by Brichon et al., silicon etching in a RIE Cl_2 plasma proceeds via the combined action of ions (Cl^+ and Cl_2^+) and neutral species (Cl and Cl_2) forming a $SiCl_x$ interface layer (approx. 0.5−4 nm).[54] The ion energy and the neutral-to-ion flux ratio (F_N/F_I) define the thickness of this interface layer (d_I) and the etch rate (Y). Importantly, for the same energy of the bombarding ions, a higher neutral-to-flux ratio was shown to enhance the etch rate. When a film and a particle are subjected to the same RIE plasma, the directional ion flux is nearly identical for both and produces a similar interfacial layer, but the isotropic flux of neutral species diffusing toward the particle surface is larger due to the exposed sides of the particle. The local enhancement of the neutral-to-ion flux ratio induces a higher etch rate for particles compared to flat films, which agrees with our findings. The etch rate may be strongly nonlinear when the size of a particle approaches the ion penetration depth ($r \leq d_I$). At that point, the particle becomes strongly doped with halogens, which facilitates its rapid removal via the formation of volatile metal halides. In addition, the fast etching of the nanosized TiO_2 nuclei might be promoted by their lower thermodynamic stability.[55]

Cyclic Plasma Halogenation Route for AS-ALD on Blanket a-C:H. To enable selective TiO_2 deposition via supercycles of $TiCl_4$/H_2O ALD, including repetitive Cl_2 or CF_4 plasma exposure (Figure 7a), the embedded plasma treatments should not modify the nucleation behavior of ALD TiO_2 on halogenated a-C:H as well as on the TiO_2 film formed on the growth surface. Therefore, we monitored the growth of TiO_2 on native SiO_2 and halogenated a-C:H after every deposition and etching step within a five-supercycle sequence. Given that the maximum efficiency of the grain removal with a CW-RIE plasma is achieved when the grain radius does not exceed the depth of ion penetration, the length of the ALD process within a supercycle should be carefully selected. Based on the previously assessed selectivity window (Figure 5a) and grain etch rates (Figure 6a), we limited each supercycle to 60 cycles of $TiCl_4$/H_2O with exposure to 10 s of Cl_2 or 15 s of CF_4 plasma. Chlorinated and fluorinated a-C:H substrates were exposed only to a Cl_2 and CF_4 plasma, respectively. The TiO_2 growth on SiO_2 was traced by ex situ ellipsometry, while the amount of TiO_2 on halogenated a-C:H was quantified by RBS and AFM (Figure 7b).

On the SiO_2 growth surface, a 2.4 nm TiO_2 film is deposited after 60 cycles of $TiCl_4$/H_2O. Successive etching in the CF_4 plasma removed about 0.3 nm TiO_2, while the thickness did

Table 1. XPS Elemental Analysis in Two Areas of the Fabricated Patterned Substrate Subjected to Plasma Halogenation—Pattern-Free Area and 60 nm Half-Pitch Line Pattern[a]

processing sequence	measurement location	C 1s (%)	N 1s (%)	O 1s (%)	Si 2p (%)	Cl 2p (%)	F 1s (%)
HM removal + chlorination	no pattern	72.0	-	8.9	1.1	18.1	-
	line pattern	45.1	2.3	26.1	12.9	13.2	0.4
HM removal + fluorination	no pattern	63.6	-	5.6	-	-	30.9
	line pattern	50.3	1.1	13.7	15.6	-	19.4

[a]The XPS atomic concentrations are presented in the angle-integrated mode (all angles summed).

not change upon exposure to the Cl_2 plasma, in agreement with the previous observations. The next supercycles showed similar etch rates and slightly reduced growth rates. The faster growth during the first supercycle can be associated with the formation of a sub-stoichiometric Ti-rich interfacial layer on native SiO_2.[56] The negligible effect of the Cl_2 plasma on the growth rate is confirmed by the same total TiO_2 thickness after five supercycles with the Cl_2 plasma and after uninterrupted deposition of 300 $TiCl_4/H_2O$ cycles (dashed line in Figure 7b). The nucleation delay observed for the fluorinated TiO_2 can be attributed to the grafting of Ti−F bonds that hydrolyze less easily than Ti−Cl bonds.[57] The combination of the nucleation delay and the faster TiO_2 etching in the CF_4 plasma resulted in 20% thinner coatings after the cyclic fluorination process. The differences in TiO_2 nucleation induced by the intermediate plasma exposure did not deteriorate the roughness of the final TiO_2 films (RMS of 0.15 nm, Figure S9).

AFM analysis on the nongrowth area allowed studying the areal TiO_2 grain density from the first supercycle, at which point the RBS Ti signal was either absent or too weak for quantification (not shown). Despite the clear reduction of the TiO_2 grain density during the etching steps, the net amount of deposited TiO_2 continued to increase with every supercycle on both fluorinated and chlorinated a-C:H. Nonetheless, there is a principal difference in the growth dynamics between the chlorination- and fluorination-based sequences. The initially superior growth inhibition on the chlorinated a-C:H is lost after three supercycles, resulting in accelerated TiO_2 nucleation. In contrast, cyclic fluorination results in a stable increase in TiO_2. These observations are linked to the different abilities of the intermediate plasma treatments to restore the halogenated a-C:H nongrowth surface (Figure 3). Accordingly, the growth-inhibiting composition of the chlorinated a-C:H surface cannot be sustained for longer than 30−40 s of Cl_2 plasma exposure, while the optimal composition of the fluorinated a-C:H surface is reached after 40 s of CF_4 plasma exposure, thus ensuring its reproducibility during multiple supercycles.

The performance of the proposed supercycle scheme was quantitatively assessed by the deposition selectivity. Analogous to the empirical definition suggested by Gladfelter,[8] we expressed selectivity S in this work via the volumes of deposited TiO_2

$$S = \frac{V_{film} - V_{grain}}{V_{film} + V_{grain}} \quad (1)$$

where V_{film} and V_{grain} correspond to the total volumes of the TiO_2 film and nuclei over an area of 2 μm^2 of the growth and nongrowth substrates, respectively. These volumes were estimated from ellipsometry and AFM grain analysis (Figure S10).

Comparing the deposition selectivity between the single-step and the supercycle halogenation process (Figure 7c) reveals that the latter was efficient only in the case of fluorination. The supercycle CF_4 plasma approach allowed for the deposition of 8 nm TiO_2 with a selectivity of 0.998, compared to 0.812 for the same number of $TiCl_4/H_2O$ cycles in a single run. The reproducibility of the fluorinated a-C:H surface during the supercycle process opens up a way to defect-free TiO_2 ASD via the optimization of the length for the deposition and etching sub-steps. The chlorination supercycle scheme fails to reduce the density of TiO_2 nuclei on the nongrowth surface compared to the continuous ALD process. The originally very high deposition selectivity of 0.999 on chlorinated a-C:H even slightly degrades due to the intermediate Cl_2 plasma steps. The potential solution could be an adjustment of the etching step by introducing a short He/H_2 or H_2 plasma treatment preceding the Cl_2 discharge. Although it would not accelerate the removal of the unwanted TiO_2 nuclei, this method could help to restore the chlorination depth as well the $-CCl_3$ terminal groups responsible for ALD TiO_2 growth suppression.

Cyclic Plasma Halogenation Route for AS-ALD on Patterned a-C:H. To demonstrate the value of cyclic halogenation for pattern inversion (Figure 1), the same supercycle process was applied to a 60 nm half-pitch line pattern of a-C:H (Figure 8a). The top- and side-wall surfaces of the a-C:H pattern have a composition distinctly different from the originally deposited a-C:H coating due to the PE-ALD SiO_2 HM deposition and N_2/H_2 plasma patterning. This difference is obvious from XPS measurements in the a-C:H line pattern area and a nonpatterned a-C:H area (Table 1). The latter is expected to give a good picture of the top surface of the a-C:H pattern because it also experienced the deposition and removal of the PE-ALD HM. Exposure to 60 s of CF_4 plasma gave a similar composition for the top surface of the pattern as for unpatterned a-C:H (Figure 2c). In contrast, 10 s of Cl_2 plasma treatment resulted in a noticeably lower chlorine content for the pattern, which additionally exhibited some traces of Si originating from the HM residues. The XPS signal of the patterned a-C:H area indicates side-wall-specific nitrogen contamination, likely introduced during patterning. Another possible source of side-wall contamination could be the re-deposition of SiO_x from the trench bottom after a-C:H layer breakthrough during the plasma patterning.

Therefore, the successful implementation of an ASD process requires the plasma halogenation treatment to have some etching capability to eliminate the contaminants as a potential source of TiO_2 nucleation defects. This point is validated by the SEM and TEM-HAADF images and TEM−EDS Ti K_α element maps recorded on the cross section of the line patterns after five supercycles (Figure 8b,c). A reference sample not subjected to any halogenation treatment was conformally coated with 9.1 nm TiO_2 after 300 $TiCl_4/H_2O$ ALD cycles. On the chlorinated a-C:H pattern, the same number of ALD cycles

in the form of five Cl_2 plasma supercycles resulted in 6.6 nm TiO_2 at the bottom of the trenches and a rough discontinuous TiO_2 layer of similar thickness on the exposed a-C:H surface. On the fluorinated a-C:H pattern, the supercycle process using the CF_4 plasma led to 3.5 nm TiO_2 exclusively on the exposed SiO_2 growth surface, which was slightly recessed following the initial 60 s fluorination step.

In comparison with the supercycle deposition on the blanket a-C:H coating, the a-C:H pattern exhibits two major differences: (1) a significant TiO_2 growth on the chlorinated a-C:H surface and (2) an increased TiO_2 etch rate resulting in a thinner layer formed at the bottom of the trenches and in the reduced density of the TiO_2 nuclei on the a-C:H surface. The first observation is directly related to the inability of the Cl_2 plasma to remove the fabrication-induced Si- and N-containing contaminants. One possible solution could be a precleaning step in the form of a short exposure to the CF_4 plasma.[58] The origin of the accelerated etching inside the trenches is not so obvious. In RIE patterning, it is more common to find a reduced etch rate inside the trenches due to the so-called loading effect consisting of the depletion of plasma radicals in the areas of high pattern density.[59] However, in this case, during the supercycle processing, the plasma etching steps are applied to an a-C:H pattern already covered with a halogen-rich layer. This could result in a locally enhanced etch rate within the trenches, as more halogen radicals would be emitted from the halogenated surfaces. Importantly, the increase in the TiO_2 etch rate did not translate into a significant etching of the a-C:H side-walls and preserved the lateral dimensions of the original pattern.

CONCLUSIONS

In summary, our study demonstrates a new scheme for the ASD of ALD TiO_2 featuring a-C:H as a base material for the growth-inhibiting layer formed and maintained by Cl_2 or CF_4 plasma treatments. We showed that the ability of the proposed approach to achieve defect-free deposition depends on the efficiency of the following three complementary selective processes: (1) selective plasma halogenation of the a-C:H in the presence of exposed oxide surfaces, that is, the formation of a stable halogen-rich layer predominantly on the a-C:H surface; (2) selective deposition of the TiO_2 film on the oxide surfaces due to the strong suppression of the metal−organic precursor chemisorption on the halogenated a-C:H surface; and (3) preferential etching of TiO_2 nuclei in the RIE plasma halogenation as compared to the continuous TiO_2 film. While the Cl_2 plasma provides outstanding selectivity in the first two processes, that is, negligible impact on the SiO_2 surface and an outstanding deposition selectivity of 0.999 in direct ALD growth of 10 nm TiO_2, the chlorination-based supercycle deposition sequence suffers from the slow TiO_2 etching and fails to maintain the optimal composition of the halogenated a-C:H surface. In contrast, the CF_4 plasma does not perform as well during the initial a-C:H halogenation and shows a deposition selectivity of only 0.812 under the same ALD TiO_2 conditions. However, the selectivity can be significantly improved through the cyclic plasma fluorination process due to the high etch capability of the CF_4 plasma and the reproducibility of the fluorinated a-C:H surface composition under prolonged plasma exposure. For 60 nm half-pitch a-C:H patterns containing fabrication-induced contaminants, the latter advantages allowed demonstrating the robustness and scalability of the proposed method. Considering its efficiency and versatility, as well as the minimal investment required for implementation in current microelectronic fabrication flows, we believe that ASD based on the cyclic halogenation of a-C:H is a valuable addition to the library of ASD technologies enabling defect-free processing.

Ternary phase diagram of carbon featuring the studied a-C:H material; process flow for the fabrication of a-C:H patterns; correlation between values of the TiO_2 layer thickness measured by RBS and spectroscopic ellipsometry; comparison of grain analysis by SEM and AFM; thermal stability of halogenated a-C:H surfaces; evaluation of the halogenated a-C:H surface stability during the ALD TiO_2 process; assessment of the growth surface wettability after halogenation; height distribution of TiO_2 nucleation defects on fluorinated a-C:H exposed to CF_4 plasma of different durations; topography images of TiO_2 films deposited on the native SiO_2 surface; and procedure for the calculation of the TiO_2 grain and film volumes (PDF)

AUTHOR INFORMATION

Corresponding Author

Rob Ameloot − *cMACS, KU Leuven, 3001 Leuven, Belgium;* orcid.org/0000-0003-3178-5480; Email: rob.ameloot@kuleuven.be

Authors

Mikhail Krishtab − *cMACS, KU Leuven, 3001 Leuven, Belgium; imec, 3001 Leuven, Belgium;* orcid.org/0000-0001-6215-8506

Silvia Armini − *imec, 3001 Leuven, Belgium;* orcid.org/0000-0003-0578-3422

Johan Meersschaut − *imec, 3001 Leuven, Belgium*

Stefan De Gendt − *imec, 3001 Leuven, Belgium; Department of Chemistry, KU Leuven, 3001 Leuven, Belgium*

Complete contact information is available at: https://pubs.acs.org/10.1021/acsami.1c04405

Notes

The authors declare no competing financial interest.

ACKNOWLEDGMENTS

The authors would like to thank Thierry Conard, Alexis Franquet, Hugo Bender, and other members of MCA group (imec) for their help with the characterization of the samples. The authors acknowledge imec's industrial affiliation program on nano-interconnects and imec's p-line for support in manufacturing of the patterned test wafers. This project received funding from the European Research Council (ERC) under the European Union's Horizon 2020 research and innovation program (grant agreement no. 716472, acronym VAPORE, and grant agreement no. 875577, acronym LO-KMOF). The authors acknowledge the Research Foundation Flanders (FWO Vlaanderen) for projects G85720N, 1501618N, G0E6319N, and G0H0716N and KU Leuven for the research project C32/18/056.

REFERENCES

(1) Moore, G. E. Cramming More Components Onto Integrated Circuits. *Proc. IEEE* **1998**, *86*, 82−85.

(2) Khan, H. N.; Hounshell, D. A.; Fuchs, E. R. H. Science and Research Policy at the End of Moore's Law. *Nat. Electron.* **2018**, *1*, 14−21.

(3) Salahuddin, S.; Ni, K.; Datta, S. The Era of Hyper-Scaling in Electronics. *Nat. Electron.* **2018**, *1*, 442−450.

(4) Mulkens, J.; Hanna, M.; Wei, H.; Vaenkatesan, V.; Megens, H.; Slotboom, D. Overlay and Edge Placement Control Strategies for the 7nm Node Using EUV and ArF Lithography. *Extreme Ultraviolet Lithogr.* **2015**, *9422*, 94221Q.

(5) Clark, R.; Tapily, K.; Yu, K.-H.; Hakamata, T.; Consiglio, S.; O'Meara, D.; Wajda, C.; Smith, J.; Leusink, G. Perspective: New Process Technologies Required for Future Devices and Scaling. *APL Mater.* **2018**, *6*, 058203.

(6) Parsons, G. N.; Clark, R. D. Area-Selective Deposition: Fundamentals, Applications, and Future Outlook. *Chem. Mater.* **2020**, *32*, 4920−4953.

(7) Carlsson, J.-O. Selective Vapor-Phase Deposition on Patterned Substrates. *Crit. Rev. Solid State Mater. Sci.* **1990**, *16*, 161−212.

(8) Gladfelter, W. L. Selective Metalization by Chemical Vapor Deposition. *Chem. Mater.* **1993**, *5*, 1372−1388.

(9) George, S. M. Atomic Layer Deposition: An Overview. *Chem. Rev.* **2010**, *110*, 111−131.

(10) Johnson, R. W.; Hultqvist, A.; Bent, S. F. A Brief Review of Atomic Layer Deposition: From Fundamentals to Applications. *Mater. Today* **2014**, *17*, 236−246.

(11) Mackus, A. J. M.; Bol, A. A.; Kessels, W. M. M. The Use of Atomic Layer Deposition in Advanced Nanopatterning. *Nanoscale* **2014**, *6*, 10941−10960.

(12) Parsons, G. N. Functional Model for Analysis of ALD Nucleation and Quantification of Area-Selective Deposition. *J. Vac. Sci. Technol., A* **2019**, *37*, 020911.

(13) Cao, K.; Cai, J.; Chen, R. Inherently Selective Atomic Layer Deposition and Applications. *Chem. Mater.* **2020**, *32*, 2195−2207.

(14) Jeong, S.-J.; Kim, J. Y.; Kim, B. H.; Moon, H.-S.; Kim, S. O. Directed Self-Assembly of Block Copolymers for next Generation Nanolithography. *Mater. Today* **2013**, *16*, 468−476.

(15) Hu, H.; Gopinadhan, M.; Osuji, C. O. Directed Self-Assembly of Block Copolymers: A Tutorial Review of Strategies for Enabling Nanotechnology with Soft Matter. *Soft Matter* **2014**, *10*, 3867.

(16) Ren, J.; Zhou, C.; Chen, X.; Dolejsi, M.; Craig, G. S. W.; Rincon Delgadillo, P. A.; Segal-Peretz, T.; Nealey, P. F. Engineering the Kinetics of Directed Self-Assembly of Block Copolymers toward Fast and Defect-Free Assembly. *ACS Appl. Mater. Interfaces* **2018**, *10*, 23414−23423.

(17) Mackus, A. J. M.; Merkx, M. J. M.; Kessels, W. M. M. From the Bottom-Up: Toward Area-Selective Atomic Layer Deposition with High Selectivity. *Chem. Mater.* **2019**, *31*, 2−12.

(18) Hashemi, F. S. M.; Bent, S. F. Sequential Regeneration of Self-Assembled Monolayers for Highly Selective Atomic Layer Deposition. *Adv. Mater. Interfaces* **2016**, *3*, 1600464.

(19) Mameli, A.; Merkx, M. J. M.; Karasulu, B.; Roozeboom, F.; Kessels, W. M. M.; MacKus, A. J. M. Area-Selective Atomic Layer Deposition of SiO_2 Using Acetylacetone as a Chemoselective Inhibitor in an ABC-Type Cycle. *ACS Nano* **2017**, *11*, 9303−9311.

(20) Merkx, M. J. M.; Vlaanderen, S.; Faraz, T.; Verheijen, M. A.; Kessels, W. M. M.; Mackus, A. J. M. Area-Selective Atomic Layer Deposition of TiN Using Aromatic Inhibitor Molecules for Metal/Dielectric Selectivity. *Chem. Mater.* **2020**, *32*, 7788−7795.

(21) Vallat, R.; Gassilloud, R.; Eychenne, B.; Vallée, C. Selective Deposition of Ta_2O_5 by Adding Plasma Etching Super-Cycles in Plasma Enhanced Atomic Layer Deposition Steps. *J. Vac. Sci. Technol., A* **2017**, *35*, 01B104.

(22) Vallat, R.; Gassilloud, R.; Salicio, O.; El Hajjam, K.; Molas, G.; Pelissier, B.; Vallée, C. Area Selective Deposition of TiO_2 by Intercalation of Plasma Etching Cycles in PEALD Process: A Bottom up Approach for the Simplification of 3D Integration Scheme. *J. Vac. Sci. Technol., A* **2019**, *37*, 020918.

(23) Song, S. K.; Saare, H.; Parsons, G. N. Integrated Isothermal Atomic Layer Deposition/Atomic Layer Etching Supercycles for Area-Selective Deposition of TiO_2. *Chem. Mater.* **2019**, *31*, 4793−4804.

(24) Vos, M. F. J.; Chopra, S. N.; Verheijen, M. A.; Ekerdt, J. G.; Agarwal, S.; Kessels, W. M. M.; Mackus, A. J. M. Area-Selective Deposition of Ruthenium by Combining Atomic Layer Deposition and Selective Etching. *Chem. Mater.* **2019**, *31*, 3878−3882.

(25) Saare, H.; Song, S. K.; Kim, J.-S.; Parsons, G. N. Effect of Reactant Dosing on Selectivity during Area-Selective Deposition of TiO_2 via Integrated Atomic Layer Deposition and Atomic Layer Etching. *J. Appl. Phys.* **2020**, *128*, 105302.

(26) Soethoudt, J.; Grillo, F.; Marques, E. A.; van Ommen, J. R.; Tomczak, Y.; Nyns, L.; Van Elshocht, S.; Delabie, A. Diffusion-Mediated Growth and Size-Dependent Nanoparticle Reactivity during Ruthenium Atomic Layer Deposition on Dielectric Substrates. *Adv. Mater. Interfaces* **2018**, *5*, 1800870.

(27) Grillo, F.; Soethoudt, J.; Marques, E. A.; de Martín, L.; Van Dongen, K.; van Ommen, J. R.; Delabie, A. Area-Selective Deposition of Ruthenium by Area-Dependent Surface Diffusion. *Chem. Mater.* **2020**, *32*, 9560−9572.

(28) Kakuchi, M.; Hikita, M.; Tamamura, T. Amorphous Carbon Films as Resist Masks with High Reactive Ion Etching Resistance for Nanometer Lithography. *Appl. Phys. Lett.* **1986**, *48*, 835−837.

(29) Pauliac-Vaujour, S.; Brianceau, P.; Comboroure, C.; Faynot, O. Improvement of High Resolution Lithography by Using Amorphous Carbon Hard Mask. *Microelectron. Eng.* **2008**, *85*, 800−804.

(30) Antonelli, G. A.; Reddy, S.; Subramonium, P.; Henri, J.; Sims, J.; O'loughlin, J.; Shamma, N.; Schlosser, D.; Mountsier, T.; Guo, W.; Sawin, H. Patterning with Amorphous Carbon Thin Films. *ECS Meet. Abstr.* **2011**, *35*, 701−716.

(31) Roy, R. K.; Choi, H.-W.; Park, S.-J.; Lee, K.-R. Surface Energy of the Plasma Treated Si Incorporated Diamond-like Carbon Films. *Diamond Relat. Mater.* **2007**, *16*, 1732−1738.

(32) Yun, D. Y.; Choi, W. S.; Park, Y. S.; Hong, B. Effect of H_2 and O_2 Plasma Etching Treatment on the Surface of Diamond-like Carbon Thin Film. *Appl. Surf. Sci.* **2008**, *254*, 7925−7928.

(33) Sainio, S.; Nordlund, D.; Caro, M. A.; Gandhiraman, R.; Koehne, J.; Wester, N.; Koskinen, J.; Meyyappan, M.; Laurila, T. Correlation between Sp^3-to-Sp^2 Ratio and Surface Oxygen Functionalities in Tetrahedral Amorphous Carbon (Ta-C) Thin Film Electrodes and Implications of Their Electrochemical Properties. *J. Phys. Chem. C* **2016**, *120*, 8298−8304.

(34) Caro, M. A.; Aarva, A.; Deringer, V. L.; Csányi, G.; Laurila, T. Reactivity of Amorphous Carbon Surfaces: Rationalizing the Role of Structural Motifs in Functionalization Using Machine Learning. *Chem. Mater.* **2018**, *30*, 7446−7455.

(35) Zyulkov, I.; Krishtab, M.; De Gendt, S.; Armini, S. Selective Ru ALD as a Catalyst for Sub-Seven-Nanometer Bottom-up Metal Interconnects. *ACS Appl. Mater. Interfaces* **2017**, *9*, 31031−31041.

(36) Stevens, E.; Tomczak, Y.; Chan, B. T.; Altamirano Sanchez, E.; Parsons, G. N.; Delabie, A. Area-Selective Atomic Layer Deposition of TiN, TiO_2, and HfO_2 on Silicon Nitride with Inhibition on Amorphous Carbon. *Chem. Mater.* **2018**, *30*, 3223−3232.

(37) Meersschaut, J.; Vandervorst, W. High-Throughput Ion Beam Analysis at Imec. *Nucl. Instrum. Methods Phys. Res., Sect. B* **2017**, *406*, 25−29.

(38) Lee, S. Y.; Lyu, J.; Kang, S.; Lu, S. J.; Bielawski, C. W. Ascertaining the Carbon Hybridization States of Synthetic Polymers with X-Ray Induced Auger Electron Spectroscopy. *J. Phys. Chem. C* **2018**, *122*, 11855−11861.

(39) Aarik, J.; Aidla, A.; Mändar, H.; Sammelselg, V. Anomalous Effect of Temperature on Atomic Layer Deposition of Titanium Dioxide. *J. Cryst. Growth* **2000**, *220*, 531−537.

(40) Nečas, D.; Klapetek, P. Gwyddion: An Open-Source Software for SPM Data Analysis. *Open Phys.* **2012**, *10*, 181−188.

(41) Schneider, C. A.; Rasband, W. S.; Eliceiri, K. W. NIH Image to ImageJ: 25 Years of Image Analysis. *Nat. Methods* **2012**, *9*, 671−675.

(42) Erradi, A.; Clergereaux, R.; Gaboriau, F. H-Atom Interaction with Amorphous Hydrocarbon Films: Effect of Surface Temperature, H Flux and Exposure Time. *J. Appl. Phys.* **2010**, *107*, 093305.
(43) Włoch, J.; Terzyk, A. P.; Wiśniewski, M.; Kowalczyk, P. Nanoscale Water Contact Angle on Polytetrafluoroethylene Surfaces Characterized by Molecular Dynamics-Atomic Force Microscopy Imaging. *Langmuir* **2018**, *34*, 4526−4534.
(44) Colorado, R.; Lee, T. R. Wettabilities of Self-Assembled Monolayers on Gold Generated from Progressively Fluorinated Alkanethiols. *Langmuir* **2003**, *19*, 3288−3296.
(45) Rakhimova, T. V.; Lopaev, D. V.; Mankelevich, Y. A.; Rakhimov, A. T.; Zyryanov, S. M.; Kurchikov, K. A.; Novikova, N. N.; Baklanov, M. R. Interaction of F Atoms with SiOCH Ultra-Low-k Films: I. Fluorination and Damage. *J. Phys. D: Appl. Phys.* **2015**, *48*, 175203.
(46) Rakhimova, T. V.; Lopaev, D. V.; Mankelevich, Y. A.; Kurchikov, K. A.; Zyryanov, S. M.; Palov, A. P.; Proshina, O. V.; Maslakov, K. I.; Baklanov, M. R. Interaction of F Atoms with SiOCH Ultra Low-k Films. Part II: Etching. *J. Phys. D: Appl. Phys.* **2015**, *48*, 175204.
(47) Sinha, A.; Hess, D. W.; Henderson, C. L. Area Selective Atomic Layer Deposition of Titanium Dioxide: Effect of Precursor Chemistry. *J. Vac. Sci. Technol., B: Microelectron. Nanometer Struct.–Process., Meas., Phenom.* **2006**, *24*, 2523.
(48) Sinha, A.; Hess, D. W.; Henderson, C. L. Transport Behavior of Atomic Layer Deposition Precursors through Polymer Masking Layers: Influence on Area Selective Atomic Layer Deposition. *J. Vac. Sci. Technol., B: Microelectron. Nanometer Struct.–Process., Meas., Phenom.* **2007**, *25*, 1721.
(49) Haider, A.; Yilmaz, M.; Deminskyi, P.; Eren, H.; Biyikli, N. Nanoscale Selective Area Atomic Layer Deposition of TiO_2 Using E-Beam Patterned Polymers. *RSC Adv.* **2016**, *6*, 106109−106119.
(50) Jur, J. S.; Spagnola, J. C.; Lee, K.; Gong, B.; Peng, Q.; Parsons, G. N. Temperature-Dependent Subsurface Growth during Atomic Layer Deposition on Polypropylene and Cellulose Fibers. *Langmuir* **2010**, *26*, 8239−8244.
(51) Thian, D.; Yemane, Y. T.; Xu, S.; Prinz, F. B. Methodology for Studying Surface Chemistry and Evolution during the Nucleation Phase of Atomic Layer Deposition Using Scanning Tunneling Microscopy. *J. Phys. Chem. C* **2017**, *121*, 27379−27388.
(52) Seo, S.; Yeo, B. C.; Han, S. S.; Yoon, C. M.; Yang, J. Y.; Yoon, J.; Yoo, C.; Kim, H.-j.; Lee, Y.-b.; Lee, S. J.; Myoung, J.-M.; Lee, H.-B. -R.; Kim, W.-H.; Oh, I.-K.; Kim, H. Reaction Mechanism of Area-Selective Atomic Layer Deposition for Al_2O_3 Nanopatterns. *ACS Appl. Mater. Interfaces* **2017**, *9*, 41607−41617.
(53) Lee, J.; Efremov, A.; Lee, B. J.; Kwon, K.-H. Etching Characteristics and Mechanisms of TiO2 Thin Films in CF_4 + Ar, Cl_2 + Ar and HBr + Ar Inductively Coupled Plasmas. *Plasma Chem. Plasma Process.* **2016**, *36*, 1571−1588.
(54) Brichon, P.; Despiau-Pujo, E.; Mourey, O.; Joubert, O. Key Plasma Parameters for Nanometric Precision Etching of Si Films in Chlorine Discharges. *J. Appl. Phys.* **2015**, *118*, 053303.
(55) Li, W.; Ni, C.; Lin, H.; Huang, C. P.; Shah, S. I. Size Dependence of Thermal Stability of TiO_2 Nanoparticles. *J. Appl. Phys.* **2004**, *96*, 6663−6668.
(56) Bronneberg, A. C.; Höhn, C.; van de Krol, R. Probing the Interfacial Chemistry of Ultrathin ALD-Grown TiO_2 Films: An In-Line XPS Study. *J. Phys. Chem. C* **2017**, *121*, 5531−5538.
(57) Buslaev, Y. A.; Dyer, D. S.; Ragsdale, R. O. Hydrolysis of Titanium Tetrafluoride. *Inorg. Chem.* **1967**, *6*, 2208−2212.
(58) Krishtab, M.; Hung, J.; Koret, R.; Turovets, I.; Shah, K.; Rangarajan, S.; Warad, L.; Zhang, V.; Ameloot, R.; Armini, S. Plasma Halogenated A-C:H as Growth Inhibiting Layer for ASD of Titanium Oxide. In *Metrology, Inspection, and Process Control for Microlithography XXXIV*; Adan, O., Robinson, J. C., Eds.; SPIE, 2020; p 27.
(59) Mogab, C. J. The Loading Effect in Plasma Etching. *J. Electrochem. Soc.* **1977**, *124*, 1262−1268.